Synthesis of high-performance MnO$_x$/carbon composite as lithium-ion battery anode by a facile co-precipitation method: Effects of oxygen stoichiometry and carbon morphology

Rung-Chuan Lee [a], Yen-Po Lin [b], Yu-Ting Weng [a], Hsiao-An Pan [a], Jyh-Fu Lee [c], Nae-Lih Wu [a],*

[a] Department of Chemical Engineering, National Taiwan University, Taipei 106, Taiwan, ROC
[b] Industrial Technology Research Institute (ITRI), Hsinchu, Taiwan, ROC
[c] National Synchrotron Radiation Research Center, Hsinchu 300, Taiwan, ROC

HIGHLIGHTS

- MnO$_x$/C composite powders are prepared by co-precipitation followed by calcination.
- Two C materials, including carbon black (CB) and graphitic flake (GF), are used.
- Effects of temperature and C on performance as Li ion battery anode are studied.
- GF benefits oxide reduction and oxide/C contact, enhancing capacity and cycle life.
- MnO/GF shows capacity of 580 mAh g^{-1}-(oxide + C) without fading after 150 cycles.

ARTICLE INFO

ABSTRACT

Manganese oxide/carbon (MnO$_x$/C) composite powders showing high performance as lithium-ion battery anode are synthesized by a facile co-precipitation process followed by thermal calcination between 400 °C and 700 °C in N$_2$, where the as-deposited MnO$_2$ is reduced progressively to Mn$_3$O$_4$ and then to MnO. The role of conductive additive is investigated by adopting two carbon (C) materials of different dimensionalities, including carbon black (CB) nanoparticles and micron-sized graphitic flakes (GFs). For MnO$_x$/CB composite, the cycling stability is remarkably enhanced with increasing calcination temperature, and this is due to increasing content of MnO, which exhibits superior redox reversibility than the oxides having higher Mn valences. Attempt to achieve single-phase MnO at higher temperature (700 °C), nevertheless, leads to deteriorated cycle performance because of the formation of large oxide particles having poor contact with CB. The use of the two-dimensional GFs creates the "balls-on-plate" oxide-C configuration. This configuration facilitates MnO formation at lower temperature and simultaneously enables retention of good oxide-C contact, leading to significantly enhanced cycling stability and rate performance. The MnO$_x$/GF composites obtained by calcination at 500−600 °C show specific capacities of 550−600 mAh g^{-1}-(oxide + C) with no capacity fading after 150 cycles.

© 2013 Elsevier B.V. All rights reserved.

1. Introduction

Lithium-ion batteries (LIBs) are expected to continue playing important roles in energy storage for mobile communication and electric vehicle (EV) and renewable energy applications in the foreseeable future. Graphite as a commercial anode material for LIB possesses the advantages of high coulombic efficiency and good cycle stability [1]. However, its theoretical capacity is only 372 mAh g^{-1}, and the demand for higher energy capacity of the energy storage cell has been driving the development of alternative anode materials with higher capacities [2]. Certain nanocrystalline metal oxides have been shown to be able to work as reversible anodes through heterogeneous conversion reaction [3,4]:

$$MO_x + 2x\, Li^+ + 2x\, e^- \leftrightarrow M + x Li_2O.$$
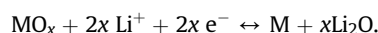
The high theoretical capacity and density give metal oxides the edge over graphite as high energy density anodes for LIB.

Nevertheless, due to the high kinetic barrier of the conversion reaction at room temperature [4,5], metal oxide anodes typically exhibit large potential hysteresis between lithiation and delithiation cycles. The hysteresis reduces the operating voltage window as well as the energy efficiency of the LIB cell. Furthermore, the poor conductivity and large volume expansion arising from lithiation of the metal oxide particles are major shortcomings that may cause poor cycling stability [6]. Compared with other conversion-type metal oxide anodes, manganese oxide (MnO_x) shows smaller potential hysteresis [7] and lower operation potential [8]. In addition, MnO_x has the advantages of being environment friendly and abundant.

Although previous studies using various synthesis methods have demonstrated the importance of applying C conductive additives in improving the overall performance of the oxide anodes, they simply used one single type of C or carbon coating to claim the improvement resulting from the addition of the C additive [9–20]. Potential impacts of C morphology and oxide-C contact pattern on the efficiency of the improvement have not been illustrated. Moreover, most of these processes involved high-temperature treatment of the synthesized Mn oxide powders [16–20]. The heat treatment may change the powder characteristics, including phase composition, oxygen stoichiometry and particle morphology, and result in different performance as conversion anode. The interplay among these powder characteristics and anode performance has mostly been neglected in the literature.

In this work, MnO_x/C composite powders have been synthesized by a facile co-precipitation process followed by thermal calcination. MnO_2 is initially formed via self-redox reaction between Mn ions of different valences in a solution where C additive is in presence. Two types of C additives with different dimensionalities, including carbon black (CB) nanoparticles and graphitic flakes (GFs), are used. This co-precipitation process has frequently been adopted in making MnO_2-based supercapacitor electrode but not yet for LIB anode [21–23]. A comprehensive study has been carried out to elucidate the interplay among the calcination conditions, powder properties, and the electrochemical performance as LIB anode.

2. Experimental

MnO_x/C composites were synthesized via a co-precipitation/calcination process. In the first step, two types of carbon additives have been adopted, including nano-sized CB (Super P, TIMCAL) and GFs (KS-6, TIMCAL). To deposit the oxide, the following procedure was adopted: the C material was first ground and then dispersed in a 150 ml aqueous solution of 0.15 M $MnSO_4$ with stirring for 1 h. Another solution containing 100 ml $KMnO_4$ (0.15 M) was added into the solution drop by drop at 25 °C until a Mn(VII)/Mn(II) molar ratio of 2:3 was reached. A dark-brownish precipitate was formed in the solution and the solution was stirred for another 1 h. At the end of sedimentation of the resulting product, the upper clear portion of the solution was decanted and replaced with de-ionized water. The same washing procedure was repeated several times. Finally, the solution was filtered and the product was dried at 50 °C. The amount of the C additive was to give a weight ratio, on the dry basis, of MnO_2:C = 80:20 in the precipitated powder. The composites will be referred to as the MnO_x/CB and MnO_x/GF hereafter for those containing CB and GF, respectively. In the second step, the composites were calcined at selected temperatures between 400 °C and 700 °C in N_2 atmosphere for 2 h.

Particle morphology was examined by scanning electron microscopy (SEM; JEOL JSM-7600F) and transmission electron microscope (TEM; JOEL JEM-1230), while crystal structure and phase composition were identified by X-ray diffraction (XRD) on a diffractometer (Rigaku, Ultima IV) with Cu Kα X-ray radiation. C content in the calcined powder was analyzed by elemental analysis (Heraeus Vario El-III).

For electrochemical characterization, the electrodes were prepared by conventional slurry-coating method on Cu foil. The active layer consisted of the MnO_x-containing composite, additional C additive, and binder (polyvinylidene difluoride, Aldrich) with a weight ratio of 83:7:10. The electrodes were dried at 120 °C for 6 h in vacuum. The resulting electrodes were assembled together with Li-foil counter electrodes to make CR2032 coin cells, and the electrolyte was 1 M $LiPF_6$ in a 1:2 (v/v) mixture of ethylene carbonate (EC) and ethyl methyl carbonate (EMC) with 2 wt.% vinylene carbonate (VC) as additive. All the cells were assembled in a dry room where the dew point was maintained at between −40 and −45 °C. The active layers had a mass of ca. 2.0 mg cm^{-2}. Electrochemical characterization was measured by constant-current charge/discharge (C/D) tests, which were carried out with selected current rates between 2.8 and 0.01 V at room temperature on a battery tester (Arbin, model: MCN6410).

Synchrotron X-ray absorption near-edge structure (XANES) analysis was conducted with the 17-C1 for XANES facilities of the National Synchrotron Radiation Research Center in Taiwan. In-operando analysis was carried out on Al pouch cells. The spectra were acquired during the course of a constant current charge/discharge cycle with a current density of 50 mA g^{-1} between 0.01 and 2.8 V with 30 min-interval. The collected data were further analyzed by using the IFEFFIT program [24].

3. Results and discussion

3.1. Powder characterization

The phase compositions of the composite powders subjected to thermal treatment were identified by XRD. For MnO_x/CB composite (Fig. 1a), the freshly deposited powder showed only weak peaks of ε-MnO_2. After heat treatment, the oxide component turned into single-phased Mn_3O_4 at 400 °C, to a mixture of Mn_3O_4 and MnO at 500 °C and 600 °C, and finally to MnO, which has the lowest oxygen stoichiometry among crystalline Mn oxides, at 700 °C. Overall, the oxygen stoichiometry of the oxide phase decreased with increasing calcination temperature.

For the MnO_x/GF composite (Fig. 1b), the freshly deposit also showed peaks of ε-MnO_2, along with strong (002) peak of graphite. Upon thermal treatment, the oxide turned into single-phase Mn_3O_4 at 400 °C, to a mixture of Mn_3O_4 and MnO at 500 °C and finally to single-phase MnO at 600 °C and 700 °C. Compared with MnO_x/CB, the MnO_x/GF powder achieves single-phase MnO at a lower temperature (600 °C versus 700 °C).

The amounts of the oxides of different oxygen stoichiometries in the mixtures may be quantitatively resolved based on XANES analysis. In this method, as shown in Fig. 2, the XANES spectrum of each oxide mixture is fitted by linear combination of the spectra of its constituent oxides, namely MnO and Mn_3O_4 [25–27]. As summarized in Table 1, for MnO_x/CB, the 500 °C and 600 °C powders exhibit essentially the same XANES spectrum, which can be assigned to the composition (in molar ratio) of Mn_3O_4:MnO = 65:35. For MnO_x/GF, the mixture after calcination at 500 °C has Mn_3O_4:MnO = 40:60, which has a higher MnO content than its MnO_x/CB counterpart. Therefore, it may be concluded that, after calcination at the same temperature of either 500 °C or 600 °C, the MnO_x/GF powders were reduced to a greater extent and hence had a higher MnO content than their MnO_x/CB counterparts. The data may suggest that the reduction process is not due solely to the intrinsic thermal stability of the oxides but also due to reduction by the C component so that the extent of reduction is affected by the type of C additive adopted. Table 1 summarizes the C contents of
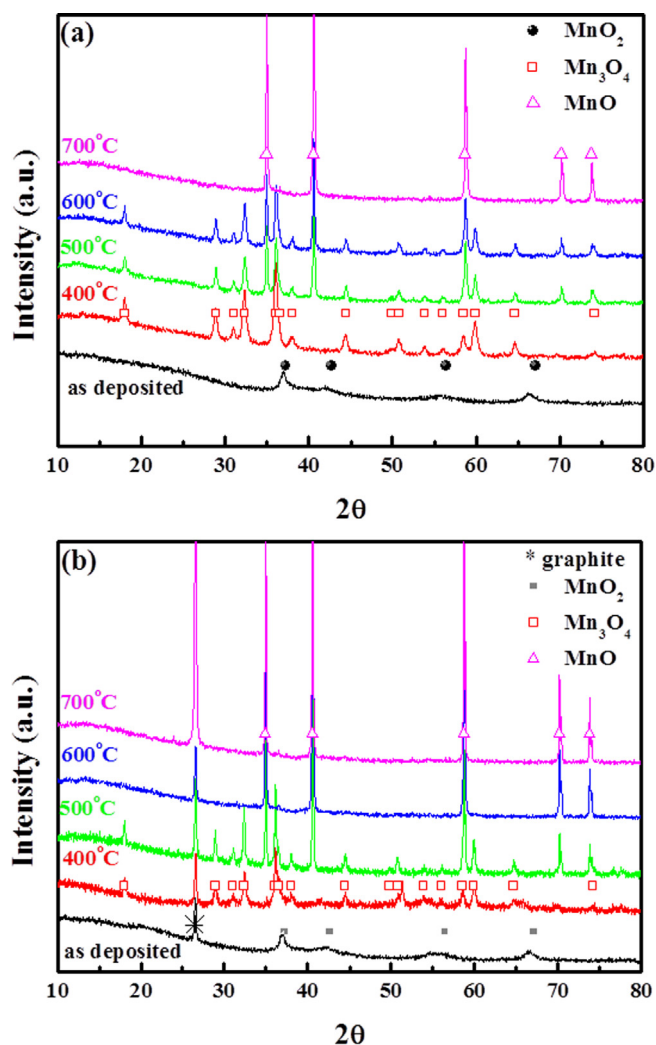
Fig. 1. XRD patterns of (a) MnO_x/CB and (b) MnO_x/GF composite powders after calcination in N_2 for 2 h between 400 °C and 700 °C.
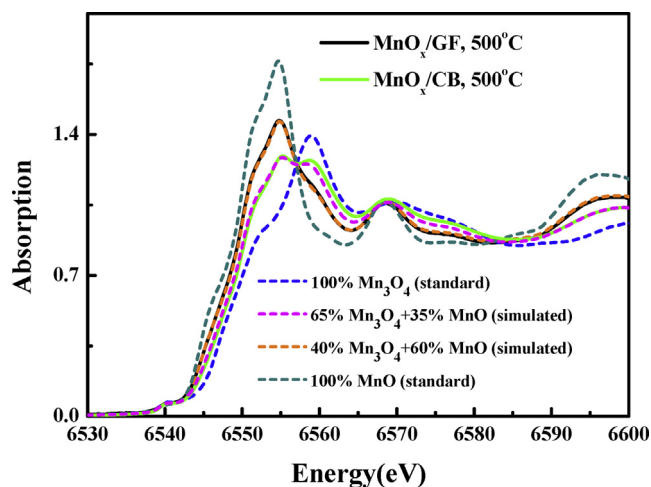

Fig. 2. Determination of phase composition of Mn oxide mixture based on XANES analysis. Shown are spectra of MnO_x/CB and MnO_x/GF 500 °C-powders (solid) and simulated spectra (dashed) assuming linear combination of standard spectra of MnO and Mn_3O_4.

Table 1
Compositions of MnO_x/C composite powders.

| Sample name	Oxide phase[a] (molar ratio)	Carbon content[b] (wt.%)
MnO_x/CB-400 °C	Mn_3O_4	18.1
MnO_x/CB-500 °C	Mn_3O_4:MnO = 65:35	19.2
MnO_x/CB-600 °C	Mn_3O_4:MnO = 65:35	18.5
MnO_x/CB-700 °C	MnO	18.4
MnO_x/GF-400 °C	Mn_3O_4	19.1
MnO_x/GF-500 °C	Mn_3O_4:MnO = 40:60	18.9
MnO_x/GF-600 °C	MnO	18.0
MnO_x/GF-700 °C	MnO	18.0

[a] Oxide phase composition is determined based on XRD and XANES analyses.
[b] Carbon content is determined by EA.

calcined powders. As shown, the final C content in general decreases with increasing calcination temperature with the exception of MnO_x/CB-400 °C powder, which has a relatively lower C content and may contain excessive amount of hydroxyl species. It is worth mentioning that theoretical final C contents of 23 wt.% and 18 wt.% are expected respectively for non- and complete participation of the C component in MnO_2-to-MnO reduction, i.e.,

$$MnO_2 \rightarrow MnO + 1/2O_2$$

and

$$MnO_2 + 1/2C \rightarrow MnO + 1/2CO_2.$$
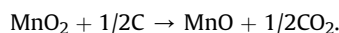
Therefore, based on the C content data shown in Table 1, it may be concluded that the C component play a very important role in the reduction process of the Mn oxide species.

The CB nanoparticles have sizes of ca. 30 nm (Fig. 3a). The co-deposited MnO_2/CB exhibited agglomerates containing MnO_2 nano-plates (Fig. 3b). Only small amount of CB particles were observed on the oxide surfaces and hence majority of them were dispersed within the interior of the oxide agglomerates. After heating at 400 °C (2 h in N_2), the MnO_x nanoplates turned into rounded particles of ca. 10 nm in diameter (Fig. 3c). The oxide particles continued to coalescence into larger particles of ca. 100 nm, 280 nm and 300 nm after heating at 500 °C, 600 °C, and 700 °C (Fig. 3d–f), respectively. Meanwhile, the sintering process of the oxide particles led to local segregation of the CB particles from the oxide particles. Many of the large oxide particles were in contact with either none or only a few CB particles. Overall, the extent of the contact between Mn oxide and CB particles became increasingly worsened with increasing calcination temperature.

The GFs (Fig. 4a) are a few microns in width and ca. 0.1 μm in thickness. The freshly deposited MnO_2/GF composite powders consisted of MnO_2 nanoplates conformally coating the GFs (Fig. 4b), and the morphology showed not much change after calcination at 400 °C (Fig. 4c). Upon calcination at 500 °C, the oxide turned into rounded particles with diameters within 20–50 nm firmly staying on the GF surfaces (Fig. 4d,e). Calcination at 600 °C produced clusters of irregular-shaped oxide particles of ca. 100–200 nm in size staying on the GF surfaces (Fig. 4f). Comparison between the oxide particle sizes of the MnO_x/GF calcined powders and those of their MnO_x/CB counterparts (Fig. 3) indicates that the extent of sintering (i.e., oxide size growth) is significantly suppressed in the MnO_x/GF powders. Calcination at 700 °C resulted in oxide particle growth and detachment from the GF surfaces (Fig. 4g,h).

Fig. 5 illustrates the TEM micrographs of the MnO_x/GF powder after calcination at 500 °C, where the MnO_x particles are shown to strongly stick to either side of a single GF. Fig. 6 schematically summarizes the effect of the morphology of the C additive on the oxide-C contact pattern after calcination. The use of the two-
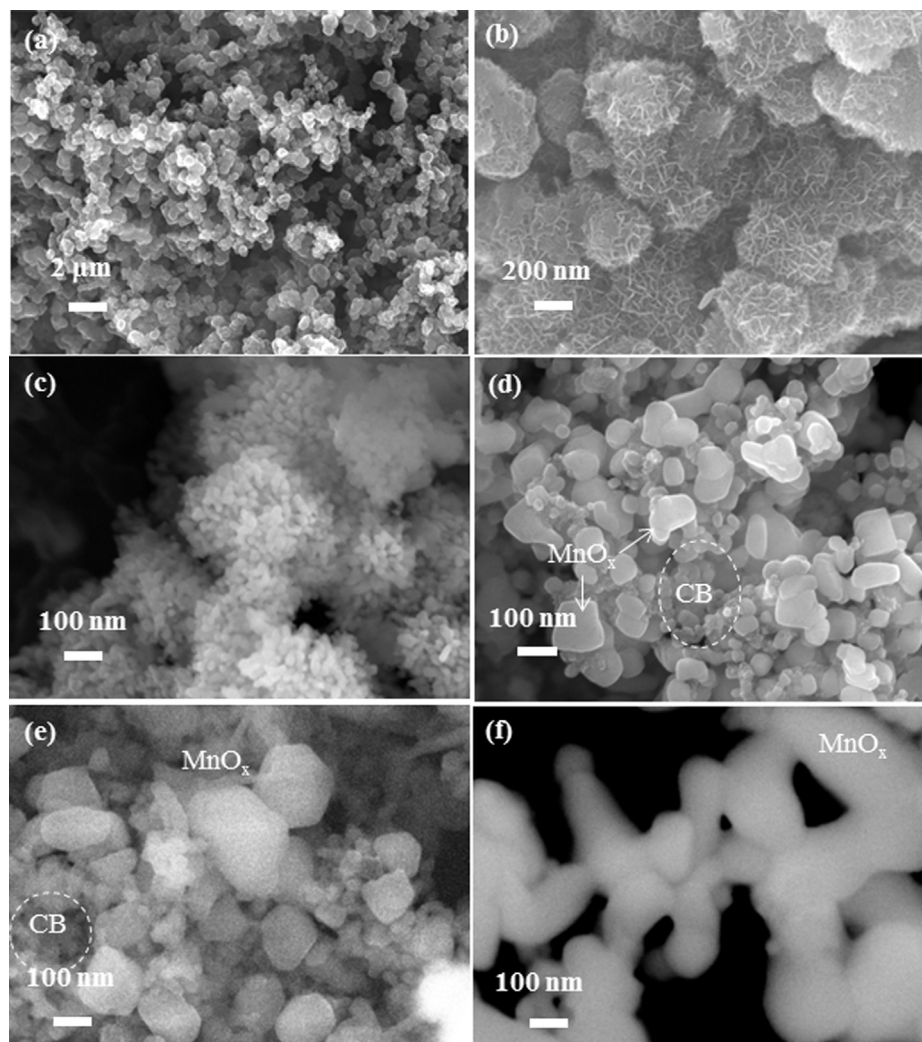
Fig. 3. SEM micrographs of MnO$_x$/CB composite powders: (a) CB powder; (b) as-deposited; (c) calcination at 400 °C, (d) 500 °C, (e) 600 °C and (f) 700 °C.

dimensional graphite flakes creates the "balls-on-plate" oxide-C configuration, suppressing particle size growth and allowing intimate oxide-C (graphite) contact after calcination. In contrast, the oxide easily grows into large particles in the case MnO$_x$/CB, causing local segregation of CB particles and deteriorated contact between the oxide and CB particles. Moreover, it is inferred that the good contact between the oxide particles and graphite surfaces at high temperatures facilitates oxide reduction by C (graphite) so that, as described earlier, the MnO$_x$/GF powders are reduced to a greater extent than their MnO$_x$/CB counterparts upon calcination at the same temperatures.

3.2. Electrochemical characterizations

The first-cycle voltage profiles of the electrodes containing MnO$_x$/CB powders subjected to different calcination temperatures are shown in Fig. 7a. The specific capacities are based on the total mass of the composite (i.e., oxide + C). By taking into account of the XRD and XANES data presented above and related data in the literature [28,29], the nature of different plateaus can be identified. For the discharge (lithiation) curve of the MnO$_x$/CB-400 °C electrode (For brevity, the electrodes will hereafter be referred to according to the calcination temperatures of the composite powders

they contain.), the plateau at 1.4 V may be attributed to the conversion from Mn$_3$O$_4$ to MnO. A small plateau at 0.8 V is attributed to the formation of solid-electrode interphase (SEI), while a long plateau at 0.38 V is to the conversion reaction from MnO to Mn. Finally, a tail is observed to extend toward 0.01 V. While it is commonly observed on the MnO$_x$ anode, the nature of the tail remains controversial. Recent in-operando XANES study [29] suggests that this part of capacity might be associated with both Mn and non-Mn reactivity (such as capacitance at nanoparticle surface [5]). The capacity contribution of the Mn$_3$O$_4$-to-MnO plateau decreases with increasing calcination temperature due to reducing amount of Mn$_3$O$_4$; it no longer occurs in the case of MnO$_x$/CB-700 °C electrode, which contains single-phase MnO. The voltage of the MnO-to-Mn plateau decreases slightly from 0.40 V to 0.25 V with increasing calcination temperature from 400 °C to 700 °C, and this variation may be caused by polarization associated with large oxide particles and deteriorated oxide-C contact. Upon charging, the voltage profiles of all the MnO$_x$/CB electrodes show redox events corresponding to those in the discharge profiles. A sloped curve that corresponds to the discharge tail first occurs to account for approximately one-third of the total charge capacity before reaching the Mn-to-MnO plateau at ca. 1.2 V. The voltage hysteresis between the MnO–Mn redox couple is 0.8–0.95 V, depending on
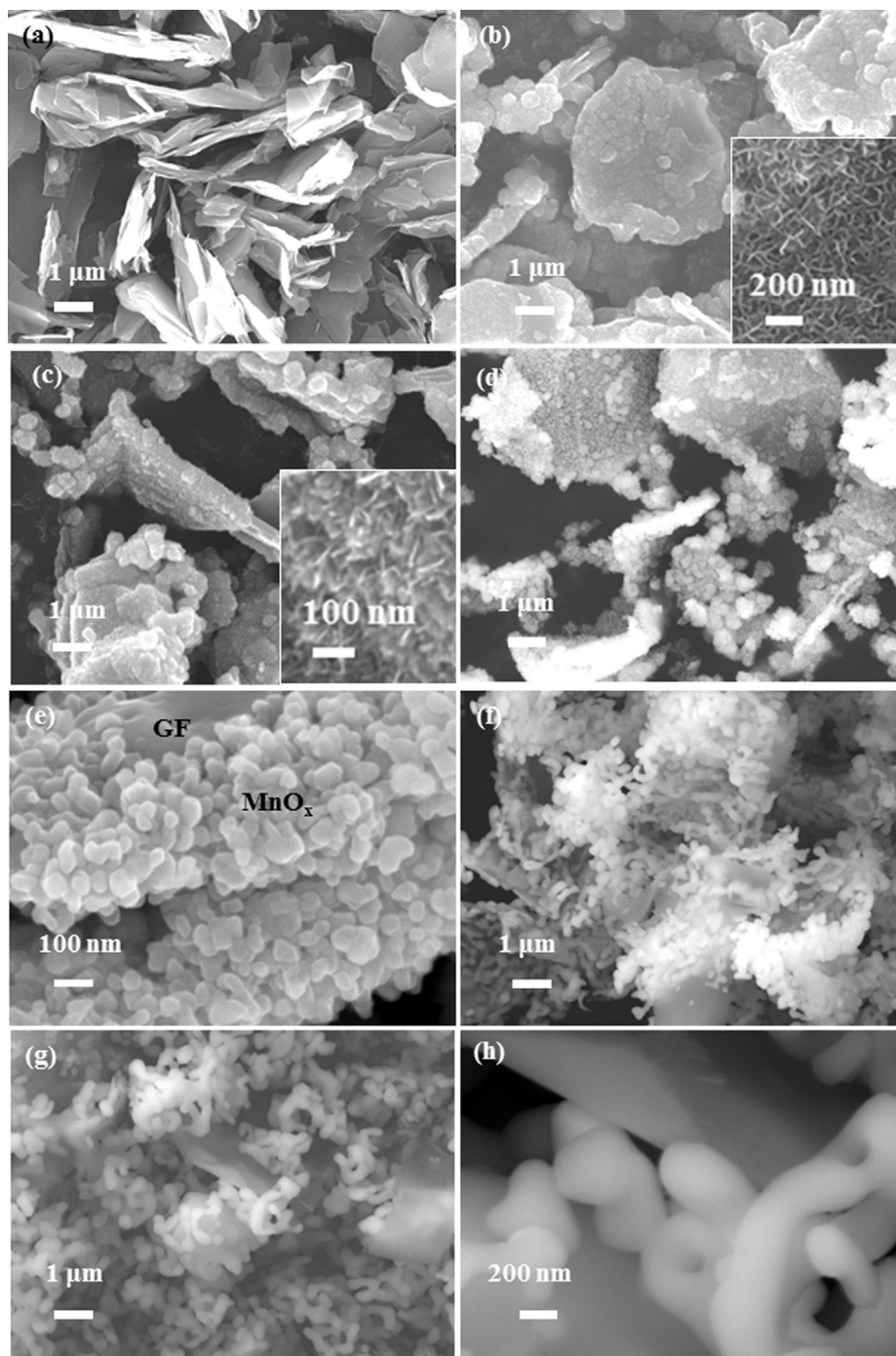
Fig. 4. SEM micrographs of MnO$_x$/GF composite powders: (a) Graphitic flakes; (b) as-deposited; (c) calcination at 400 °C, (d,e) 500 °C, (f) 600 °C and (g,h) 700 °C. The insets show micrographs at higher magnifications.

the polarization of the electrode. A small sloped plateau corresponding to MnO-to-Mn$_3$O$_4$ conversion can be seen above 2.0 V for the 400 °C and 500 °C electrodes.

For the MnO$_x$/GF-400 °C electrode (Fig. 7b), there is a slope extending from 2.5 V to 1.5 V, and the occurrence of this slope may suggest the presence of small amount of MnO$_2$ impurity, in spite of its essentially single-phase Mn$_3$O$_4$ XRD pattern. Below 1.5 V, the profile is similar to that of the MnO$_x$/CB 400 °C-electrode, showing a small Mn$_3$O$_4$-to-MnO plateau at ca. 1.4 V and a major MnO-to-Mn plateau at ca. 0.4 V. The Mn$_3$O$_4$–MnO conversion plateau once again diminishes with increasing calcination temperature, leaving

only the MnO-to-Mn conversion plateau for the 600 °C electrode. The plateau associated with lithiation of the graphite component cannot be individually identified. Nevertheless, upon charging, a small plateau due to de-lithiation of the graphite can be clearly identified at ca. 0.15 V. The Mn-to-MnO oxidation plateau is observed at ca. 1.2 V, while the MnO-to-Mn$_3$O$_4$ plateau does not occur during the first cycle.

For all electrodes, the first-cycle coulombic efficiencies are low. The irreversible capacities may originate from three different sources. The first source is the SEI formation, which accounts for the plateau at ca. 0.8 V. The second source is the irreversible conversion
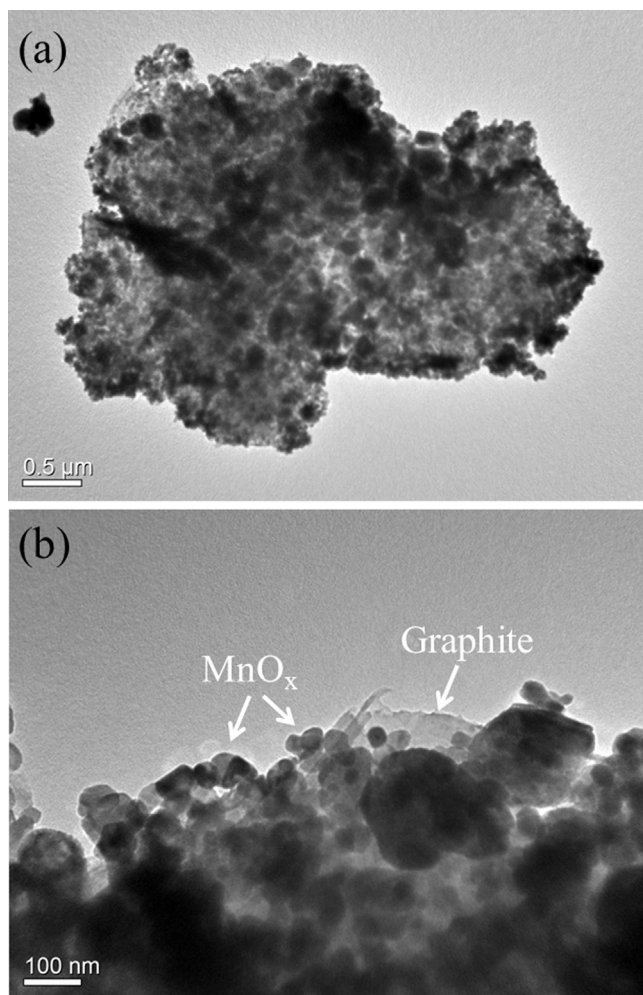
Fig. 5. TEM micrographs of the MnO_x/GF composite calcined at 500 °C.

Fig. 7. First-cycle charge/discharge voltage profiles of (a) MnO_x/CB electrodes and (b) MnO_x/GF electrodes.

between MnO_x ($x > 1$) to MnO during first cycle, particularly for the samples with high O/Mn ratios. As shown in Fig. 7, first de-lithiation produces primarily MnO but not any other oxide, such as Mn_3O_4, with higher oxygen stoichiometry. The third source might originate from incomplete reversible conversion reaction between MnO and

Fig. 6. Schematics showing changes in MnO_x–C contact patterns upon calcination for (a) MnO_x/CB and (b) MnO_x/GF composite powders.
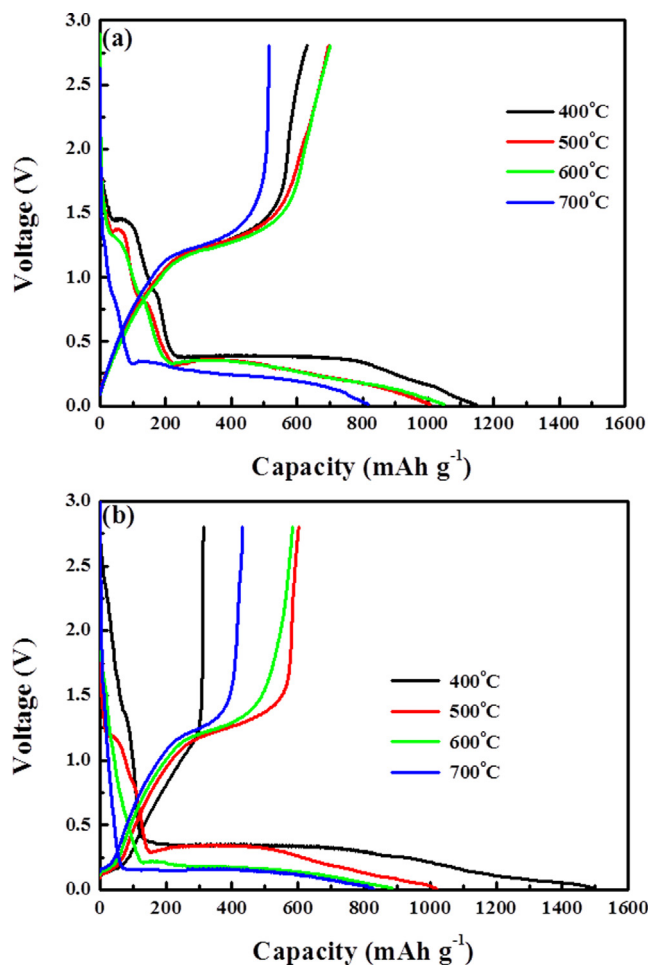
Mn due to loss of electric contacts of individual active material particles.

The cycle performance of different MnO_x/CB electrodes is summarized in Fig. 8a. The capacity of the 400 °C electrode faded rapidly. The cycling stability, nevertheless, improved significantly when the calcination temperature was raised to 500 °C and 600 °C but rapidly deteriorated again to 700 °C. This trend can be explained by taking into consideration of two factors, namely the oxygen stoichiometry and the oxide-C contact pattern. As indicated by the voltage profiles shown in Fig. 7, the MnO–Mn_3O_4 redox is largely irreversible during initial cycles. A high Mn_3O_4 content may lead to the presence of excessive insulating Li_2O, which would deteriorate the electronic conductivity of the electrode and hence leads to poor cycle life. Therefore, the cycle stability increases with increasing calcination temperature due to reduction in overall oxygen stoichiometry. The improved cycling performance for the 500 °C and 600 °C electrodes over the 400 °C one is hence due to the fact that they have lower Mn_3O_4 contents. Calcination at 700 °C, although further reducing oxygen content to give single-phase MnO, leads to extensive sintering of the oxide particles, causing poor oxide-C contact. The cycling performance becomes worsened because of deteriorated conductivity of the electrode. Finally, both the 500 °C and 600 °C electrodes show capacity rise after considerable number of cycles; this will be discussed later.

MnO_x/GF electrodes also show remarkable improvement in cycling stability when the calcination temperature is increased
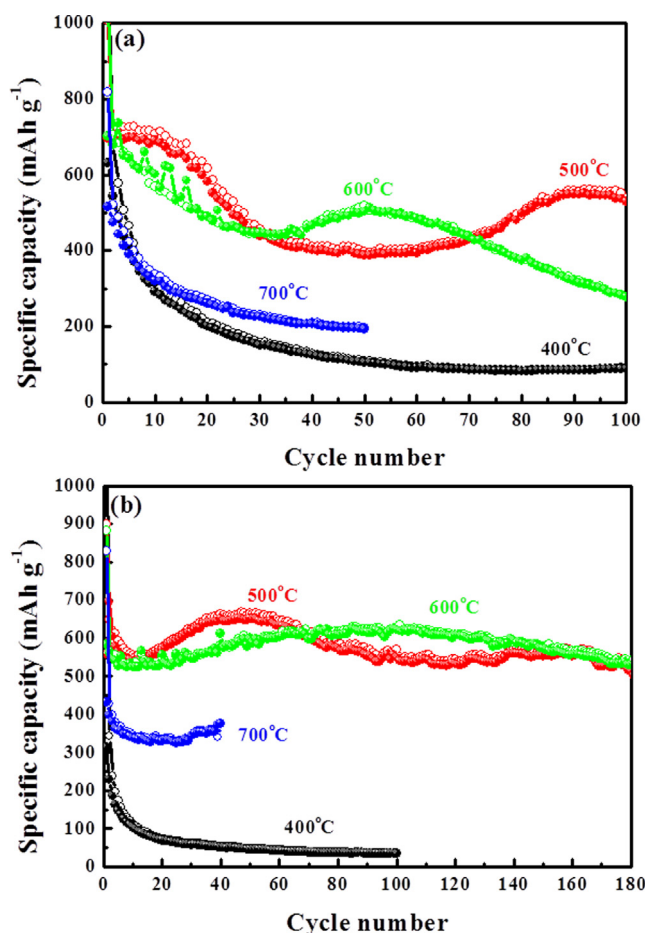
Fig. 8. Cycle performance for (a) MnO$_x$/CB electrodes and (b) MnO$_x$/GF electrodes (current density: 50 mA g^{-1}; open symbols: discharge capacity; solid: charge capacity).

Fig. 9. Charge/discharge voltage profiles of selected cycles for (a) MnO$_x$/CB-500 °C electrode and (b) MnO$_x$/GF-500 °C electrode.

from 400 °C to 500 °C (Fig. 8b). Moreover, for calcination temperatures of 500 °C and 600 °C, the MnO$_x$/GF electrodes exhibit superior cycling stability than the MnO$_x$/CB electrodes. The formers exhibit stable capacities of 550–600 mAh g^{-1}-(MnO$_x$ + GF) after a few initial cycles and retain the same capacities after 150 cycles (Fig. 8b). The causes to such differences may be twofold. On the one hand, the MnO$_x$/GF electrodes have lower Mn$_3$O$_4$ than their counterparts (Fig. 1). In particular, the MnO$_x$/GF-600 °C powder already showed single-phase MnO. On the other hand, the oxide particles in the MnO$_x$/GF electrodes remained stick to the surfaces of the GFs (Fig. 4), which may provide highly conducting pathways. This is vividly different from the MnO$_x$/CB particles, where CB particles segregated locally as the smaller oxide particles coalesced into larger particles. Calcination of MnO$_x$/GF at 700 °C leads to deterioration in both capacity and cycling stability (Fig. 8b).

It is interesting to note in Fig. 8 that, for the 500 °C- and 600 °C-electrodes of both types of composite powders, the capacity rises up after considerable number of cycles. Fig. 9a shows the voltage profiles of selected cycles of the MnO$_x$/CB 500 °C-electrode, which exhibits capacity-rise between the 60th and 100th cycles. Comparing the charge profiles of the 60th and 100th cycles indicates that the capacity rise originates from the development of the MnO–Mn$_3$O$_4$ conversion at ca. 2.0 V. Similarly, capacity rise occurs between the 12th and 45th cycles for the MnO$_x$/GF-500 °C electrode, and the charge voltage profiles also indicate the development of the MnO–Mn$_3$O$_4$ plateau (Fig. 9b). The nature of the plateau is further confirmed by in-operando XANES study. Fig. 10
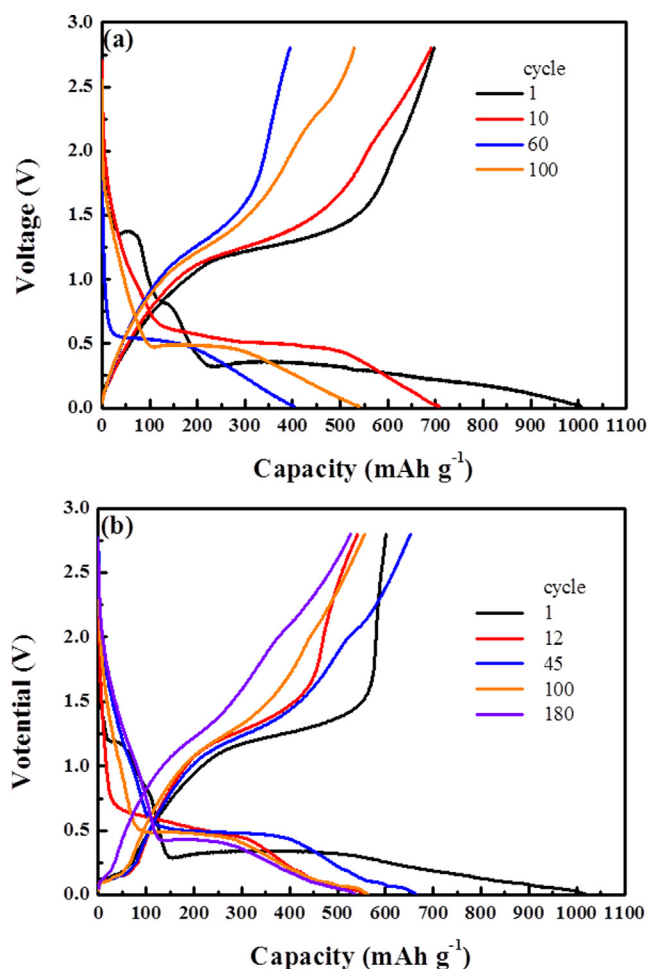
shows the XANES spectra taken during charge from 2.0 V to 2.8 V of a MnO$_x$/GF-500 °C electrode during the 101th cycle. The two-phase reaction nature of MnO–Mn$_3$O$_4$ conversion is indicated by the occurrence of an isosbestic point at 6556 eV. On either side of this point, one sees graduate intensity reduction of the peak at
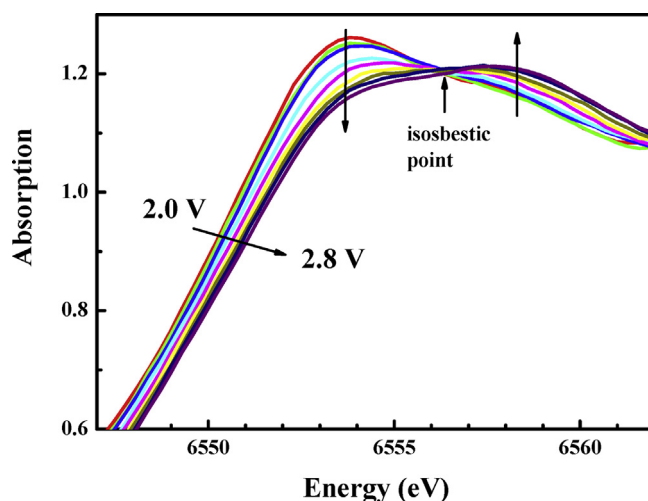

Fig. 10. In-operando XANES spectra taken on a MnO$_x$/GF-500 °C electrode during charging from 2.0 V to 2.8 V.

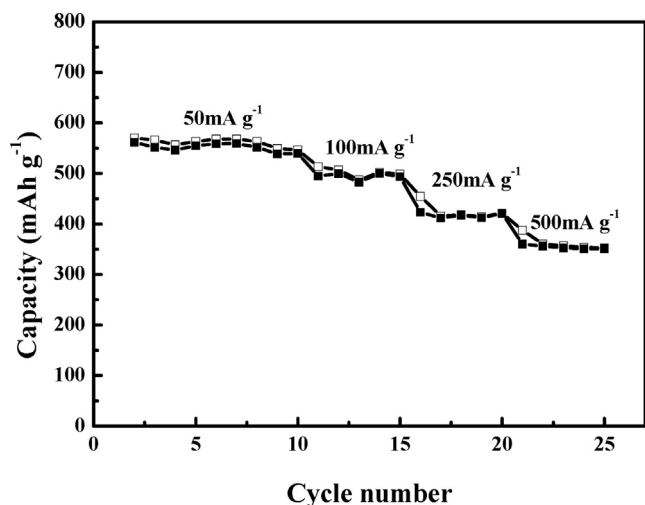**Fig. 11.** Rate performance of MnO$_x$/GF-500 °C electrode.

6553 eV, characteristic of MnO, and intensity increase of the peak at 6558 eV, characteristic of Mn$_3$O$_4$, with increasing voltage. The detail of the in-operando XANES analysis over the entire voltage range will be reported in a future publication. Lowe [29] once suggested that reversible lithiation conversion only takes place between MnO and Mn, while our data indicates that the reaction can be extended to between MnO and Mn$_3$O$_4$. It is interesting to note that even in the case of MnO$_x$/GF 600 °C-electrode, which contains single-phase MnO, exhibits gradual development of MnO–Mn$_3$O$_4$ conversion after prolonged cycling. In this case, some metallic Mn may become inactive, perhaps due to losing contact with the conductive framework of the electrode, and the excess oxygen atoms further oxidize MnO to Mn$_3$O$_4$ upon charge to higher voltages.

Finally, Fig. 11 shows the rate performance of the MnO$_x$/GF-500 °C electrode, which shows 64% capacity retention (ca. 360 mAh g^{-1}) when the current density is increased by 10 times from 50 to 500 mA g^{-1}. While this electrode exhibits similar cycling performance to the MnO$_x$/GF-600 °C electrode, it possesses superior rate performance because of its small oxide particle size and the balls-on-plate configuration, providing intimate contact between the oxide particles and GF substrate (Fig. 4d,e).

4. Conclusions

MnO$_x$/C composite powders used as lithium-ion battery anode were synthesized by a facile co-precipitation process followed by thermal calcination treatment between 400 °C and 700 °C in N$_2$, where the as-deposited MnO$_2$ was reduced progressively to Mn$_3$O$_4$ and then to MnO. The role of C additive was investigated by adopting two C additives of different dimensionalities, including CB nanoparticles with 30 nm size and GFs with micron-size in width. The interplay among calcination condition, powder characteristics, including oxide composition, morphology, and the oxide-C contact pattern, and the electrochemical performance has been studied. For MnO$_x$/CB composite, the cycling stability was found to first increase with increasing calcination temperature up to 500–600 °C, and this is due to increasing content of MnO, which exhibits superior redox

reversibility than Mn$_3$O$_4$. Attempt to achieve single-phase MnO in MnO$_x$/CB at higher temperature (700 °C) led to deteriorated cycle performance because of formation of large oxide particles having poor contact with the CB particles. The use of the two-dimensional GFs creates the "balls-on-plate" oxide-C configuration, allowing intimate oxide-C (graphite) contact upon calcination. This facilitates MnO formation at lower temperature and simultaneously enables retention of good oxide-C contact, leading to greater cycling stability. The MnO$_x$/GF composites obtained by calcination at 500–600 °C showed specific capacity of 550–600 mAh g^{-1}-(oxide + C) with no capacity fading after 150 cycles.

References

[1] M. Endo, C. Kim, K. Nishimura, T. Fujino, K. Miyashita, Carbon 38 (2000) 183–187.
[2] R. Marom, S.F. Amalraj, N. Leifer, D. Jacob, D. Aurbach, J. Mater. Chem. 21 (2011) 9938–9954.
[3] P. Poizot, S. Laruelle, S. Grugeon, L. Dupont, J.M. Tarascon, Nature 407 (2000) 496–499.
[4] P. Poizot, S. Laruelle, S. Grugeon, L. Dupont, J.M. Tarascon, J. Power Sources 97–98 (2001) 235–239.
[5] H. Li, P. Balaya, J. Maier, J. Electrochem. Soc. 151 (2004) A1878–A1885.
[6] J.-G. Kang, Y.-D. Ko, J.-G. Park, D.-W. Kim, Nanoscale Res. Lett. 3 (2008) 390–394.
[7] X.Q. Yu, Y. He, J.P. Sun, K. Tang, H. Li, L.Q. Chen, X.J. Huang, Electrochem. Commun. 11 (2009) 791–794.
[8] P. Poizot, S. Laruelle, S. Grugeon, J.M. Tarascon, J. Electrochem. Soc. 149 (2002) A1212–A1217.
[9] K. Zhong, X. Xia, B. Zhang, H. Li, Z. Wang, L. Chen, J. Power Sources 195 (2010) 3300–3308.
[10] C.-T. Hsieh, C.-Y. Lin, J.-Y. Lin, Electrochim. Acta 56 (2011) 8861–8867.
[11] L. Ji, A.J. Medford, X. Zhang, J. Mater. Chem. 19 (2009) 5593–5601.
[12] A. Yu, H.W. Park, A. Davies, D.C. Higgins, Z. Chen, X. Xiao, J. Phys. Chem. Lett. 2 (2011) 1855–1860.
[13] S.-Y. Liu, J. Xie, Y.-X. Zheng, G.-S. Cao, T.-J. Zhu, X.-B. Zhao, Electrochim. Acta 66 (2012) 271–278.
[14] Y.J. Mai, D. Zhang, Y.Q. Qiao, C.D. Gu, X.L. Wang, J.P. Tu, J. Power Sources 216 (2012) 201–207.
[15] Y.J. Mai, S.J. Shi, D. Zhang, Y. Lu, C.D. Gu, J.P. Tu, J. Power Sources 204 (2012) 155–161.
[16] J. Liu, Q. Pan, Electrochem. Solid-State Lett. 13 (2010) A139–A142.
[17] C. Chae, J.H. Kim, J.M. Kim, Y.-K. Sun, J.K. Lee, J. Mater. Chem. 22 (2012) 17870–17877.
[18] Y. Liu, X. Zhao, F. Li, D. Xia, Electrochim. Acta 56 (2011) 6448–6452.
[19] B. Sun, Z. Chen, H.-S. Kim, H. Ahn, G. Wang, J. Power Sources 196 (2011) 3346–3349.
[20] Y.L. Ding, C.Y. Wu, H.M. Yu, J. Xie, G.S. Cao, T.J. Zhu, X.B. Zhao, Y.W. Zeng, Electrochim. Acta 56 (2011) 5844–5848.
[21] H.Y. Lee, J.B. Goodenough, J. Solid State Chem. 144 (1999) 220–223.
[22] S.-L. Kuo, N.-L. Wu, J. Electrochem. Soc. 153 (2006) A1317–A1324.
[23] C.J. Hung, J.H. Hung, P. Lin, T.Y. Tseng, J. Electrochem. Soc. 158 (2011) A942–A947.
[24] B. Ravel, M. Newville, J. Synchrotron Radiat. 12 (2005) 537–541.
[25] W.B. Kim, J.S. Lee, J. Phys. Chem. B 107 (2003) 9195–9202.
[26] E. Piskorska, K. Lawniczak-Jablonska, R. Minikayev, A. Wolska, W. Paszkowicz, P. Klimczyk, E. Benko, Spectrochim. Acta B 62 (2007) 461–469.
[27] S. Datta, A.M. Rule, J.N. Mihalic, S.N. Chillrud, B.C. Bostick, J.P. Ramos-Bonilla, I. Han, L.M. Polyak, A.S. Geyh, P.N. Breysse, Environ. Sci. Technol. 46 (2012) 3101–3109.
[28] X. Fang, X. Lu, X. Guo, Y. Mao, Y.-S. Hu, J. Wang, Z. Wang, F. Wu, H. Liu, L. Chen, Electrochem. Commun. 12 (2010) 1520–1523.
[29] M.A. Lowe, J. Gao, H.D. Abruna, J. Mater. Chem. A 1 (2013) 2094–2103.